

Insights into air cushion dynamics during drop impact on heated substrate at low impact energy

Durbar Roy¹, Srinivas Rao S¹, Vishnu Hariharan¹, and Saptarshi Basu^{1†}

¹Department of Mechanical Engineering, Indian Institute of Science, Bengaluru, 560012, India

(Received xx; revised xx; accepted xx)

We study the air layer dynamics beneath a drop impinging a heated surface at low impact energy using high-speed reflection interferometry imaging and theoretical analysis. The air film has been subdivided into two distinct disjoint regions, the central dimple and the peripheral disc. We decipher that a gaussian profile can approximate the dynamic shape evolution of the central air dimple. We further observe that the dimple geometry is a function of impact energy and its dependence on surface temperature is relatively weak. The air layer rupture time and rupture radius increases with increase in substrate temperature. We characterize the air layer profile as a 2D Knudsen field and show that a unified treatment, including continuum and non-continuum mechanics, is required to comprehend the air layer dynamics coherently. The airflow dynamics in the central dimple region falls within the purview of continuum stokes regime. In contrast, the peripheral air disc falls within the non-continuum (gas kinetic effects) slip flow and transition regime characterized by a high Knudsen number. However, the initial average air disc expansion dynamics could be understood in terms of stokes approximation. In non-continuum regimes of the peripheral air disc, we discover intriguing asymmetric interface perturbations. The asymmetric wetting of the substrate initiates at the edge of the peripheral disc region. These perturbative structures cause asymmetric wetting/contact between the droplet and the substrate. Due to the asymptotic effects of capillary and van der Waals interaction in the disc region, the sub-micron spatial structures can exist at short time scales.

Key words: Authors should not enter keywords on the manuscript, as these must be chosen by the author during the online submission process and will then be added during the typesetting process (see <http://journals.cambridge.org/data/relatedlink/jfm-keywords.pdf> for the full list)

1. Introduction

Drop impact phenomena is quite ubiquitous and spectacular. Appreciating the elegant structures that appear during drop impact dynamics on solids and liquids does not require scientific training. This phenomenon thus appears in a variety of advertisements/artistic contexts in the media industries. The physics underlying the aesthetic beauty of drop impact phenomena is equally beautiful and attracts the scientific community to study it

† Email address for correspondence: sbasu@iisc.ac.in

in various contexts. The original study of drop impact physics began with the seminal work of Worthington (Worthington 1877; Worthington *et al.* 1877; Worthington 1883) in the late nineteenth century. Using ingenious mechanical arrangements to synchronize the fall of the droplet with that of an electric discharge Worthington was able to study the drop impact phenomena on solids and liquids. Initial observations made by Worthington were manual and hand drawn. Later on, Worthington was able to record the impact phenomena on photographic plates (Worthington & Cole 1897, 1900).

With the advent of high-speed imaging, experimental drop impact physics was revolutionized as scientists and engineers could probe smaller and finer spatiotemporal scales (Thoroddsen *et al.* 2008; Yarin *et al.* 2017). The experimental research in drop impact was majorly driven by various technologies and industrial processes like inkjet printing (Wijshoff 2018; Lohse 2022), food processing industries (Andrade *et al.* 2013), spray technologies (Breitenbach *et al.* 2017, 2018) to mention a few. The landscape of outcomes of any drop impact scenario is enormous. The variety of impact outcomes depends on the impact geometry, substrate type (solid vs. liquid), ambient pressure, and surface temperature (Yarin 2006; Xu *et al.* 2005; Roy *et al.* 2019, 2023). A general drop impact phenomenon can be characterized experimentally by a set of non-dimensional numbers like Weber number, Reynolds number, Ohnesorge number, Bond number, Capillary number, and Mach number, to name a few. Each of these non-dimensional numbers represents the balance of the dominant scale related to a particular phenomenon observed during impact experiments. Some phenomena related to drop impacts are spreading, splashing, bouncing, corona formation, and various kinds of Worthington jets, to name a few. These phenomena are well studied experimentally Yarin *et al.* (2017); Thoroddsen *et al.* (2012) especially spreading and splashing due to their wide application in industries. Drop impact phenomena generally are multi-scale phenomena ranging from nano-scale (Li *et al.* 2015; De Ruiter *et al.* 2015) to millimeter scales. Despite immense research in drop impact studies from the last one and a half-century, several aspects of droplet impact physics still remain elusive and need further investigation.

One such area is the air layer dynamics beneath an impacting droplet. When a droplet approaches an impacting interface, the bottom part (leading edge) of the droplet experiences a rise in pressure due to lubrication pressure buildup. The lubrication pressure, in general, is inversely proportional to the distance between the leading edge and the impacting surface/interface. The increased pressure at the leading edge of the droplet causes a dimple and peripheral disc region to form. As the air between the droplet and substrate thins out various interactions (capillary, van der Waals) on top of lubrication effects becomes dominant. The stability of the air layer between the droplet and the impacting surface/interface depends on the interaction between capillary and van der Waals interaction. Recent experimental works have shown that droplets in the size range of millimeters are supported by micro and nano air films (Kolinski *et al.* 2012; Langley *et al.* 2017; Langley & Thoroddsen 2019). The destabilization of the air layer is inherently related to bubble formation in various drop impact systems. Bubbles in industrial and various engineering impact systems like printing, painting, and cooling are often detrimental to the optimum working efficiency of the system. However, bubbles could also be helpful, as is seen in various natural systems like raindrops impacting liquid bodies. In these natural systems, bubbles help in the gaseous exchange between the atmosphere and the liquid bodies supporting aquatic/marine life (Woolf *et al.* 2007).

On approaching the impacting surface, the droplet experiences a pressure rise at the leading edge of the droplet due to air draining beneath the droplet and the substrate. The dimple forms beneath the impacting drop when the lubrication pressure exceeds the capillary pressure. The central dimple has been explored by scientists in the last decade

experimentally and computationally (Hicks & Purvis 2010, 2011; de Ruiter *et al.* 2012; De Ruiter *et al.* 2015; de Goede *et al.* 2019; Driscoll & Nagel 2011). However, surrounding the central air dimple exists a region that we refer to as the peripheral air disc (Roy *et al.* 2022). The air layer dynamics in the peripheral region remain relatively unexplored, and scientific literature is sparse. Recently Chubynsky *et al.* (Chubynsky *et al.* 2020) shed some light on the effect of Van der Waals force related to gas kinetic effects (GKE) in drop impacts for low Weber number computationally.

In our previous work (Roy *et al.* 2022), we have explored the peripheral air disc in the context of drop impact on immiscible liquid pools. We showed new structures could exist in the peripheral air disc due to a balance of capillary and van der Waals (vdW) interaction. This work focuses on the air layer dynamics of drop impact on heated substrates at low impact energies (Weber number) below the Leidenfrost temperature. We study the dynamic evolution of the central air dimple and the peripheral air disc for different substrate temperatures ranging from 27°C to 200°C . The impact Weber number ($We = \rho_l V_0^2 R_0 / \sigma_{aw}$) based on droplet radius R_0 , liquid density ρ_l , impact velocity V_0 , and air-water surface tension σ_{aw} was kept low ($We \sim 1$) so that the effect of inertia and compressibility could be neglected. At low Weber number regime, lubrication approximation holds good. We detect non-isotropic structures in the peripheral air disc using high-speed reflection interferometric imaging. The structures in the peripheral air disc region cause asymmetric wetting between the droplet and the substrate. The film mode and the kink mode are the two fundamental contact modes designated by some recent works (de Ruiter *et al.* 2015*b,a*; Li *et al.* 2015; Langley & Thoroddsen 2019). The film mode, or the first kink mode, occurs just outside the dimple, whereas the kink mode, or the second kink mode, occurs at the maximum extension of the drop (Chubynsky *et al.* 2020). The film mode occurs for $We \gg 1$ whereas the kink mode occurs for $We \sim 1$. Based on our previous (Roy *et al.* 2022) and current work, we propose that the underlying cause of both the film and kink mode are the non-isotropic structures we discover in the peripheral air disc region.

2. Materials and Methods

We study liquid water drop impact on heated solid glass substrate below the Leidenfrost temperature. The drop on approaching the impacting surface causes lubrication pressure rise in the thin air layer between the drop and the substrate. The lubrication pressure on exceeding the capillary pressure across the drop interface results in the formation of the central air dimple and the peripheral air disc. We study the evolution of the central air dimple and the peripheral air disc using high speed imaging and theoretical analysis.

2.1. Experimental Set up

Using high-speed reflection interferometric imaging, we study the air layer dynamics beneath the impacting drop on a glass substrate at various surface temperatures. The schematic representation of the experimental setup and the alignment of the actual experimental setup is shown in Fig. 1(a) and 1(b), respectively. De-ionized water drop of radius 1.1mm is generated from a syringe pump (New Era Pump Systems, NE-1010). The drop impacts a glass substrate of dimensions $75 \times 25 \times 1\text{mm}^3$ (produced from Blue Star) with an impact velocity of 0.25m/s . The drop was allowed to fall freely under gravity from a designated height to achieve the desired impact velocity.

We used cleaned glass slides for the experiments. The glass slides were sonicated in a bath of isopropanol for 10 minutes. The glass slide was then placed on the annular-shaped heater (copper surface) connected to a PID controller for maintaining the precise

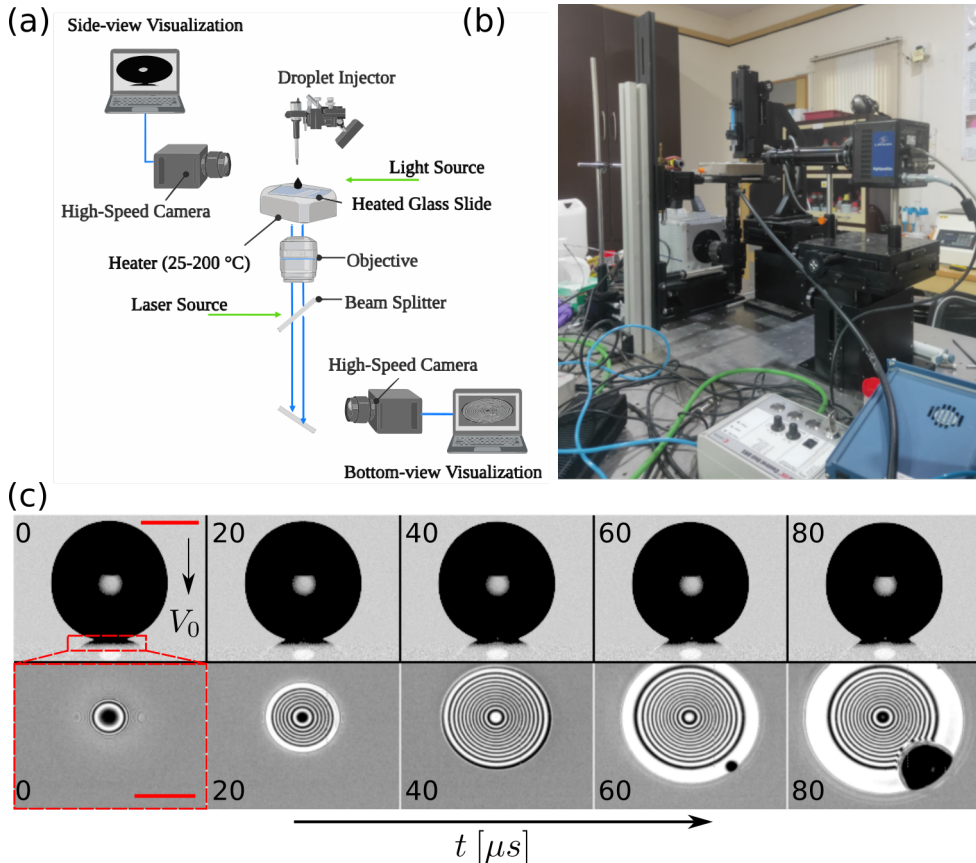


FIGURE 1. (a) Schematic of the experimental set up. (b) Actual experimental setup. (c) A typical time series depicting the side and interferometric view of an impacting drop on a substrate with $T_s = 300^\circ K$ respectively. Timestamps are in microseconds and the scale bar for the side view and interferometric view represents $1.3mm$ and $0.296mm$ respectively.

temperature conditions on the heated surface. The surface temperature of the glass plate at the impact region (placed on the annular heater) was measured using a K-type thermocouple within the error range of $\pm 5^\circ C$. We capture the drop impact phenomena using two simultaneous high speed imaging techniques (shadowgraphy and interferometry) at identical frame rates to understand and characterize the impact and the air-layer dynamics for substrate temperatures $300^\circ K$, $353^\circ K$, $423^\circ K$ and $473^\circ K$. Shadowgraphy is performed from the side view, and reflection interference imaging from the bottom view as shown in Fig. 1(a) and Fig. 1(b). For the shadowgraphy we use a LED (Light Emitting Diode) light source for backlight, a high speed camera connected with a zoom lens (Navitar). The shadowgraphy was performed at 50000 FPS (frames per second). Sample shadowgraphy and interference image sequence are shown in the top and bottom image sequence panel of Fig. 1(c) for substrate temperature $T_s = 300^\circ K$. The drop impacts the glass with a velocity $V_0 = 0.25m/s$. The dotted rectangle in the side view shows the field of view for the bottom view interferograms. The timestamps are in microseconds for both the shadowgraphy and interference image sequence. The scale bar shown in red for the side and interferometric view represents $1.3mm$ and $0.296mm$ respectively.

The reflection interference imaging setup was aligned on the bottom side of the glass

plate to record the dynamic interference patterns during drop impact. The interference system consists of a pulse-diode laser source (Cavitar Cavilux smart UHS, 400 W power, $\lambda = 640\text{nm}$) for illumination purpose; a beam-splitter; 4x microscope objective; dichoric mirror; high speed camera Fig. 1(a). The reflected light beam from the beam-splitter passes through the microscopic objective onto the glass surface. The reflected light from the top glass surface and the bottom surface of the air-water interface of the impacting drop superimposes to produce an interference pattern. The interference pattern was focused using a zoom lens (Navitar) with the assistance of the in-line alignment of the dichoric mirror, as shown in Fig 1(a). The dynamic fringe patterns were recorded using a high-speed camera (Photron SA5) with similar frame rates to the side-view imaging (i.e., at 50000 FPS). A pixel resolution of $1.5\mu\text{m}$ per pixel was used to resolve the constructive and destructive interference patterns. The present study explores the air layer dynamics at low-impact Weber number regime ($We \sim 1$) due to the dominant lubrication effects compared to the inertial and compressible effects.

2.2. Interferometry post-processing

A monochromatic beam from the diode laser source passes through the microscope objective and gets transmitted through the glass substrate. Some part of the transmitted beam suffers a reflection at the air-glass interface (top surface of the glass substrate) and travels back to the CCD of the high-speed camera with an intensity I_1 . The other part of the transmitted beam coming out of the glass substrate travels through the air layer beneath the impacting droplet and undergoes a reflection at the air-water interface (bottom surface of the impacting droplet). The reflected beam from the air-droplet interface travels back to the CCD of the high-speed camera with an intensity I_2 . Beams with intensity I_1 and I_2 superimpose to produce the interference pattern recorded by the CCD of the high-speed camera. The interference occurs because the beams I_1 and I_2 are coherent as they are derived from a single beam. Further, the beam with intensity I_2 is phase shifted to the beam with intensity I_1 due to the additional path traversed through the air layer. The path difference between beams I_1 and I_2 causes a phase shift producing a resultant interference pattern of intensity I given by (Daniel *et al.* 2017; Limozin & Sengupta 2009; Sugiyama *et al.* 2006)

$$I(x, y) = I_1 + I_2 + 2\sqrt{I_1 I_2} \cos\phi(x, y) \quad (2.1)$$

where ϕ is the phase difference between beams having intensity I_1 and I_2 . $I(x, y)$ is the resultant intensity of the interference pattern recorded by the camera CCD at an image coordinate (x, y) . Sample dynamic side views image sequence and interferograms are shown in Fig. 1(c) during drop impact on 300°K glass substrate at $We = 2$. The timestamps are in microseconds. The main feature of equation (2.1) is to represent the resultant intensity distribution on the image coordinate plane due to the interference of beams having intensity I_1 , I_2 and the cosine-modulated phase field given by $\cos\phi(x, y)$. If the phase gradient is high, high-density fringes are observed. Similarly, a smaller phase gradient corresponds to low fringe density. The dark fringes correspond to destructive interference, whereas the white fringes correspond to constructive interference. In this context, the dynamic fringe patterns during drop impingement have been processed using the fast-frequency guided sequential demodulation (FFSD) method (Kai & Kemao 2010; Wang & Kemao 2009). Fast-frequency guided algorithms are suitable for transient phenomena and consequent comprehensive extraction of the two-dimensional phase field of the complex fringe patterns. The gradient of phase distribution for the obtained fringe

patterns has been estimated from the fast-frequency guided sequential demodulation given as (Roy *et al.* 2022; Kai & Kemaio 2010):

$$\phi(x, y) = \omega(x, y)e^{i\theta(x, y)} \quad (2.2)$$

Here, $\omega(x, y)$ signifies the amplitude to determine the local frequencies precisely in the spatial domain through frequency-guided strategy, and θ denotes the angle of the complex number determined from the initial intensity variables. The obtained phase variables are constructed to be continuous and unwrapped. The height of the air-layer profiles can be estimated for the preferred wavelength of the light source λ and refractive index n of the fluid medium as (Kitagawa 2013):

$$h(x, y) = \frac{\lambda}{2\pi n} \phi(x, y) \quad (2.3)$$

The images acquired with the shadowgraphy technique (i.e., side-view imaging) were processed using a combination of open-source tools like ImageJ (Schneider *et al.* 2012) and python (Van Rossum & Drake 2009) for one on one comparison in a variation of the droplet shape during impact and simultaneous change in interference pattern for the varying surface temperatures. Sufficient number of experimental runs were conducted to ensure statistically significant datasets.

3. Results and Discussions

3.1. Global overview

Fig. 2(a) depicts the schematic and the geometry of the impact phenomenon. The air layer dynamics beneath an impacting droplet on a heated substrate at various substrate temperatures ($T_s = 300^\circ K, 353^\circ K, 423^\circ K$ and $473^\circ K$) has been studied using high-speed reflection interferometry imaging at low impact energy of $0.287\mu J$ ($We \sim 1$). The air layer beneath the droplet is subdivided into two distinct disjoint regions that we refer to as the central air dimple, surrounded by a peripheral air disc (Fig. 2(b)). Fig. 2(b) depicts the air layer profile schematically. The * denotes the central air dimple, and # represents the peripheral air disc. The thickness of the central dimple, in general, is larger than the peripheral air disc region by one order of magnitude (i.e., $h_*/h_{\#} \sim \mathcal{O}(10)$). We observe using high-speed interferometry imaging that the geometrical features features of the dimple (i.e., central dimple maximum thickness and central dimple diameter) are weakly dependent on the substrate temperature T_s and depends on the impact energy/Weber number (We) in general. We also observe that the air layer rupture time scale and rupture radius increases with the increase in the substrate temperature. Further, we show that a gaussian profile can approximate the shape of the central air dimple during its evolution. A standard continuum stokes flow regime governs the central dimple evolution. In contrast, the dynamics in the peripheral disc region falls in the non-continuum regime characterized by a relatively high value of Knudsen number (Fig. 2(c) and 2(d)). Fig. 2(c) shows a 3d wireframe plot of the air layer non-dimensional height profile at a surface temperature of $T_s = 423^\circ K$ normalized with respect to the mean free path of air. The non-dimensional height profile is a one-to-one map of the inverse Knudsen field map. The dotted rectangle in Fig. 2(b) and Fig. 2(c) depicts the interfacial perturbations in the peripheral air disc. Fig. 2(d) depicts the Knudsen contour field corresponding to Fig. 2(c). We observe intriguing 3d structures along the peripheral air disc region that acts as a seed for asymmetric wetting by the drop on the substrate. Such structural length scales exist at short time scales due to balance of capillary and molecular interactions like

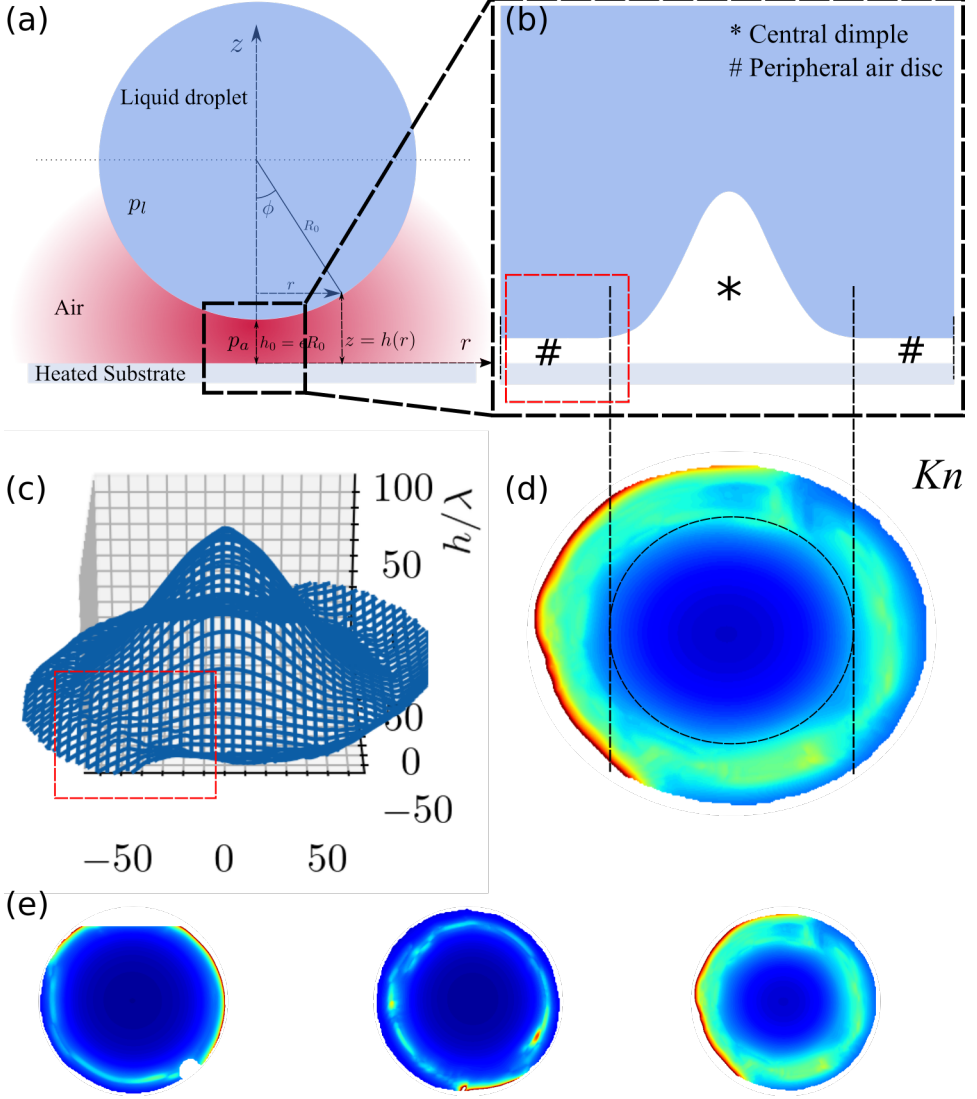


FIGURE 2. (a) Schematic representation depicting the initial impact configuration, geometry and coordinate system just before dimple formation occurs. (b) Close up schematic of the bottom most point of the droplet depicting the central air dimple (*) and the peripheral air disc (#). (c) A typical 3D non-dimensional air layer thickness profile for substrate temperature of $T_s = 423^\circ K$ depicting interface perturbations. (d) A typical Knudsen field contour map of the air layer beneath the droplet for substrate temperature of $T_s = 423^\circ K$. (e) Knudsen field just before air layer rupture/wetting of the substrate for substrate temperature of $T_s = 300^\circ K$, $T_s = 353^\circ K$, and $T_s = 423^\circ K$ respectively.

van der Waals (vdW) interactions. Fig. 2(e) depicts the Knudsen field contour map for impact on $T_s = 300^\circ K$, $T_s = 353^\circ K$ and $T_s = 423^\circ K$ respectively. We observe structures in the peripheral air disc's small annular disc region. These structures lead to asymmetric wetting between the droplet and substrate. The structures in the peripheral disc are the underlying cause of the kink and film mode of first contact between the drop and the substrate.

From section 3.2 onwards, we analyze the air layer dynamics using experimental and

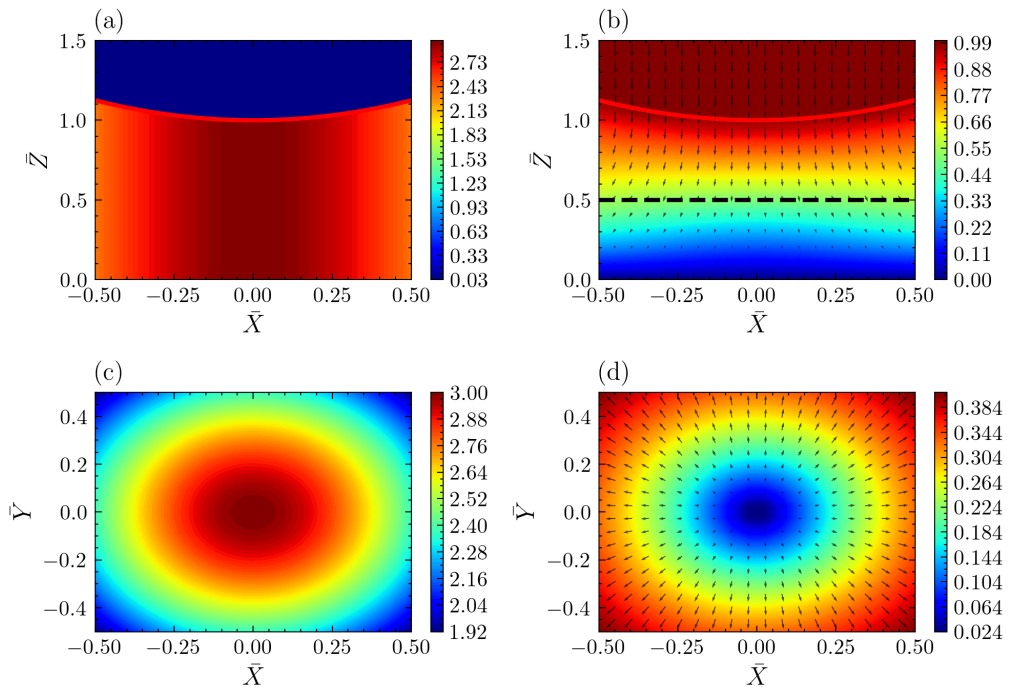


FIGURE 3. Asymptotic pressure and velocity fields just before the dimple formation. (a) Pressure field in \bar{X} , \bar{Z} plane. (b) Velocity field in \bar{X} , \bar{Z} plane. (c) Pressure field in \bar{X} , \bar{Y} plane. (d) Velocity field in \bar{X} , \bar{Y} plane at $\bar{Z} = 0.5$.

theoretical methods. We subdivide the analysis into various sub-sections. Section 3.2 introduces the coordinate system and the initial condition before dimple formation. Section 3.3 focuses on the asymptotic analysis for the velocity and pressure field in the dimple region. Section 3.4 provides an estimate of the dynamic dimple radius. Section 3.5 deals with the radial expansion of the peripheral air disc. We discuss and explore the air layer dynamics and perturbative structures in the peripheral air disc in section 3.6.

We begin the analysis by considering the geometry and initial condition for understanding air layer dynamics underneath the impacting droplet.

3.2. Coordinate system and Air profile just before dimple formation

Fig. 2(a) depicts a schematic representation of the impact geometry just before the central air dimple begins to form. We use a cylindrical coordinate system to pose the mathematical problem.

From the geometry of the droplet, we have using elementary trigonometric correlations (Fig. 2(a))

$$\sin\phi = \frac{r}{R_0}; \quad \cos\phi = \frac{\sqrt{R_0^2 - r^2}}{R_0}$$

where ϕ is an angle parametrizing the bottom surface of the droplet, r is the radial coordinate from the axis of the cylindrical coordinate system (vertical z axis), and R_0 is the impacting drop radius. The build of lubrication pressure in the air layer just before the dimple formation begins is shown schematically in red. The pressure in the liquid drop and the air layer is p_l and p_a respectively. The closest approach distance between the drop and the substrate is denoted by $h_0 = \epsilon R_0$, where ϵ is a small asymptotic parameter

that we will be used later in computing the pressure and velocity field respectively. The bottom part of the impacting drop just before the dimple formation can be approximated as part of a sphere. The initial air layer thickness profile therefore can be written as

$$z(r) = h_0 + R_0 \left(1 - \sqrt{1 - \left(\frac{r}{R_0} \right)^2} \right) \quad (3.1)$$

where $z(r)$ is the air thickness at any radius r between the drop and the substrate. h_0 is the minimum air layer thickness between the drop and the substrate before dimple formation begins to occur at the $r = 0$. Being part of a sphere, equation (3.1) is symmetric about the vertical z axis in a cylindrical coordinate system. Fig. 3(a) visualizes the drop profile along a sectional mid-plane passing through the drop centre. The red solid 1D curve in Fig. 3(a) represents the drop shape in a non-dimensional coordinate space.

3.3. Asymptotic analysis

We begin with the asymptotic analysis of the air layer beneath the impacting drop. The asymptotic analysis analyzes the pressure and the velocity field of the air layer just before the dimple starts to form in the vicinity of the origin of the cylindrical coordinate system. Equation (3.1) could be rewritten for $r \ll R_0$ using the binomial expansion (region of interest is very close to the bottom part of the droplet) as

$$z(r) = R_0\epsilon + \frac{1}{2} \frac{r^2}{R_0} \quad (3.2)$$

where $\epsilon = h_0/R_0$ is the asymptotic parameter characterizing the initial condition. Equation (3.2) depicts a parabolic (quadratic) profile approximating the bottom surface of the impacting droplet. Normalizing the air layer thickness $z(r)$ with respect to minimum thickness of the air layer just before dimple formation $h_0 = \epsilon R_0$, equation (3.2) could be written in terms of a non dimensional thickness profile \bar{z}

$$\bar{z} = \frac{z}{R_0\epsilon} = 1 + \frac{r^2}{2R_0^2\epsilon} \quad (3.3)$$

where $\bar{z} = h(\bar{r})$ represents the non-dimensional height profile of the droplet surface just before the dimple formation process. Defining a non-dimensional radial coordinate $\bar{r} = r/(R_0\epsilon^{1/2})$ equation (3.3) could be written as

$$\bar{z} = h(\bar{r}) = \frac{z}{R_0\epsilon} = 1 + \frac{1}{2}\bar{r}^2 \quad (3.4)$$

The red solid curve in Fig. 3(a) depicts equation (3.4) graphically along the sectional mid plane of the drop in cartesian coordinates $X - Z$ plane. The continuity equation in cylindrical axi-symmetric coordinates can be written as

$$\frac{1}{r} \frac{\partial}{\partial r} (ru_r) + \frac{\partial u_z}{\partial z} = 0 \quad (3.5)$$

Using $z = \bar{z}R_0\epsilon$, $r = \bar{r}R_0\epsilon^{1/2}$, $u_z = \bar{u}_z V_0$ in equation (3.5) we have

$$\frac{\epsilon^{1/2}}{V_0} \frac{1}{\bar{r}} \frac{\partial}{\partial \bar{r}} (\bar{r}u_r) + \frac{\partial \bar{u}_z}{\partial \bar{z}} = 0 \quad (3.6)$$

where V_0 is the impact velocity of the droplet. Defining $\bar{u}_r = u_r/(V_0/\epsilon^{1/2})$ the dimen-

sionless continuity equation becomes

$$\frac{1}{\bar{r}} \frac{\partial}{\partial \bar{r}} (\bar{r} \bar{u}_r) + \frac{\partial \bar{u}_z}{\partial \bar{z}} = 0 \quad (3.7)$$

The radial momentum equation in cylindrical coordinates can be written as

$$\rho_a \left(\frac{\partial u_r}{\partial t} + u_r \frac{\partial u_r}{\partial r} + u_z \frac{\partial u_r}{\partial z} \right) = -\frac{\partial p}{\partial r} + \mu_a \left(\frac{\partial^2 u_r}{\partial z^2} + \frac{1}{r} \frac{\partial}{\partial r} \left(r \frac{\partial u_r}{\partial r} \right) \right) \quad (3.8)$$

Using the scalings for $z = \bar{z} R_0 \epsilon$, $r = \bar{r} R_0 \epsilon^{1/2}$, $u_z = \bar{u}_z V_0$, $u_r = \bar{u}_r V_0 \epsilon^{-1/2}$, $t = \bar{t} R_0 \epsilon / V_0$, $p = \bar{p} \mu_a V_0 / (R_0 \epsilon^2)$ in equation (3.8) the radial momentum equation becomes

$$Re_\epsilon \left(\frac{\partial \bar{u}_r}{\partial \bar{t}} + \bar{u}_r \frac{\partial \bar{u}_r}{\partial \bar{r}} + \bar{u}_z \frac{\partial \bar{u}_r}{\partial \bar{z}} \right) = -\frac{\partial \bar{p}}{\partial \bar{r}} + \left(\frac{\partial^2 \bar{u}_r}{\partial \bar{z}^2} + \frac{\epsilon}{\bar{r}} \frac{\partial}{\partial \bar{r}} \left(\bar{r} \frac{\partial \bar{u}_r}{\partial \bar{r}} \right) \right) \quad (3.9)$$

where $Re_\epsilon = \rho R_0 V_0 \epsilon / \mu_a = Re \epsilon$. Re is the standard Reynolds number defined with respect to droplet radius R_0 , whereas Re_ϵ is the modified Reynolds number with respect to R_0 . In the limit of $\epsilon \rightarrow 0$ equation (3.9) reduces to

$$\frac{\partial^2 \bar{u}_r}{\partial \bar{z}^2} = \frac{\partial \bar{p}}{\partial \bar{r}} \quad (3.10)$$

The z momentum equation in cylindrical coordinates can be written as

$$\rho_a \left(\frac{\partial u_z}{\partial t} + u_r \frac{\partial u_z}{\partial r} + u_z \frac{\partial u_z}{\partial z} \right) = -\frac{\partial p}{\partial z} + \mu_a \left(\frac{\partial^2 u_z}{\partial z^2} + \frac{1}{r} \frac{\partial}{\partial r} \left(r \frac{\partial u_z}{\partial r} \right) \right) \quad (3.11)$$

Using the scalings for $z = \bar{z} R_0 \epsilon$, $r = \bar{r} R_0 \epsilon^{1/2}$, $u_z = \bar{u}_z V_0$, $u_r = \bar{u}_r V_0 \epsilon^{-1/2}$, $t = \bar{t} R_0 \epsilon / V_0$, $p = \bar{p} \mu_a V_0 / (R_0 \epsilon^2)$ in equation (3.11) the z momentum equation becomes

$$Re_\epsilon \epsilon \left(\frac{\partial \bar{u}_z}{\partial \bar{t}} + \bar{u}_r \frac{\partial \bar{u}_z}{\partial \bar{r}} + \bar{u}_z \frac{\partial \bar{u}_z}{\partial \bar{z}} \right) = -\frac{\partial \bar{p}}{\partial \bar{z}} + \epsilon \left(\frac{\partial^2 \bar{u}_z}{\partial \bar{z}^2} + \frac{\epsilon}{\bar{r}} \frac{\partial}{\partial \bar{r}} \left(\bar{r} \frac{\partial \bar{u}_z}{\partial \bar{r}} \right) \right) \quad (3.12)$$

In the limit of $\epsilon \rightarrow 0$ equation (3.12) reduces to

$$\frac{\partial \bar{p}}{\partial \bar{z}} = 0 \quad (3.13)$$

Integrating equation (3.10) with respect to \bar{z} twice we have

$$\bar{u}_r(\bar{r}, \bar{z}) = \frac{\partial \bar{p}}{\partial \bar{r}} \bar{z}^2 + C_1(\bar{r}) \bar{z} + C_2(\bar{r}) \quad (3.14)$$

The quantities C_1 and C_2 are evaluated from the respective boundary conditions. The continuum boundary conditions for the velocity field components are

$$\bar{u}_r = \bar{u}_z = 0; \text{ at } \bar{z} = 0 \quad (3.15)$$

$$\bar{u}_r = 0; \bar{u}_z = -1; \text{ at } \bar{z} = h(\bar{r}) \quad (3.16)$$

Evaluating C_1 and C_2 from equation (3.15) and equation (3.16); equation (3.14) for the radial velocity component reduces to

$$\bar{u}_r = \frac{\partial \bar{p}}{\partial \bar{r}} \left(\frac{\bar{z}^2}{2} - \frac{\bar{z} h(\bar{r})}{2} \right) \quad (3.17)$$

The pressure gradient term $\partial \bar{p} / \partial \bar{r}$ is still unknown at this stage and is computed from

the continuity equation (3.7). Integrating equation (3.7) with respect \bar{z} we have

$$\int_0^{h(\bar{r})} \frac{1}{\bar{r}} \frac{\partial \bar{r} \bar{u}_r}{\partial \bar{r}} d\bar{z} + \int_0^{h(\bar{r})} \frac{\partial \bar{u}_z}{\partial \bar{z}} d\bar{z} = 0 \quad (3.18)$$

$$\int_0^{h(\bar{r})} \frac{1}{\bar{r}} \frac{\partial \bar{r} \bar{u}_r}{\partial \bar{r}} d\bar{z} + \bar{u}_z|_{\bar{z}=h(\bar{r})} - \bar{u}_z|_{\bar{z}=0} = 0 \quad (3.19)$$

Applying the boundary conditions from equation (3.15) and (3.16) in equation (3.19), we have

$$\int_0^{h(\bar{r})} \frac{1}{\bar{r}} \frac{\partial \bar{r} \bar{u}_r}{\partial \bar{r}} d\bar{z} + (-1 - 0) = 0 \quad (3.20)$$

$$\int_0^{h(\bar{r})} \frac{1}{\bar{r}} \frac{\partial \bar{r} \bar{u}_r}{\partial \bar{r}} d\bar{z} = 1 \quad (3.21)$$

Substituting equation (3.17) in equation (3.21) we have

$$\frac{1}{\bar{r}} \frac{\partial}{\partial \bar{r}} \left[\bar{r} \int_0^{h(\bar{r})} \frac{\partial \bar{p}}{\partial \bar{r}} \left(\frac{\bar{z}^2}{2} - \frac{\bar{z}h(\bar{r})}{2} \right) d\bar{z} \right] = 1 \quad (3.22)$$

$$\frac{\partial \bar{p}}{\partial \bar{r}} = -\frac{6\bar{r}}{h^3(\bar{r})} + \frac{D_1}{\bar{r}h^3(\bar{r})} \quad (3.23)$$

At $\bar{r} = 0$, $\partial \bar{p} / \partial \bar{r} = 0$ (symmetry boundary condition). Therefore $D_1 = 0$

$$\frac{\partial \bar{p}}{\partial \bar{r}} = -\frac{6\bar{r}}{h^3(\bar{r})} \quad (3.24)$$

Substituting the radial pressure gradient from equation (3.24) in equation (3.17), the radial velocity could be written as

$$\bar{u}_r = -\frac{6\bar{r}}{h^3(\bar{r})} \left(\frac{\bar{z}^2}{2} - \frac{\bar{z}h(\bar{r})}{2} \right) \quad (3.25)$$

Using the undeformed asymptotic droplet shape profile $h(\bar{r}) = 1 + \bar{r}^2/2$ and integrating equation (3.24) we have

$$\bar{p}(\bar{r}) = \frac{3}{(1 + \bar{r}^2/2)^2} \quad (3.26)$$

Further, substituting the dimple profile in equation (3.25) the radial velocity becomes

$$\bar{u}_r = -\frac{6\bar{r}}{(1 + \bar{r}^2/2)^3} \left(\frac{\bar{z}^2}{2} - \frac{\bar{z}}{2}(1 + \bar{r}^2/2) \right) \quad (3.27)$$

Fig. 3 depicts the asymptotic normalized pressure and velocity fields in the air layer beneath the drop just prior to dimple formation. Fig. 3(a) represents the axisymmetric pressure field in the $\bar{X} - \bar{Z}$ cartesian plane according to equation (3.26). The respective cartesian coordinates x , y , z are expressed as non-dimensional cartesian coordinates using the scales $x = \bar{X}R_0\epsilon^{1/2}$, $y = \bar{Y}R_0\epsilon^{1/2}$, $z = \bar{Z}R_0\epsilon$. We observe from equation (3.26) that the non-dimensional pressure is maximum at the origin of coordinate system ($\bar{p}(\bar{r} = 0) = 3$). The red curve shows the asymptotic air-water droplet interface prior to dimple formation begins according to equation (3.4). The actual experimental value of ϵ observed was $\epsilon = 1.146 \times 10^{-3}$. Fig. 3(b) represents the asymptotic velocity field data in

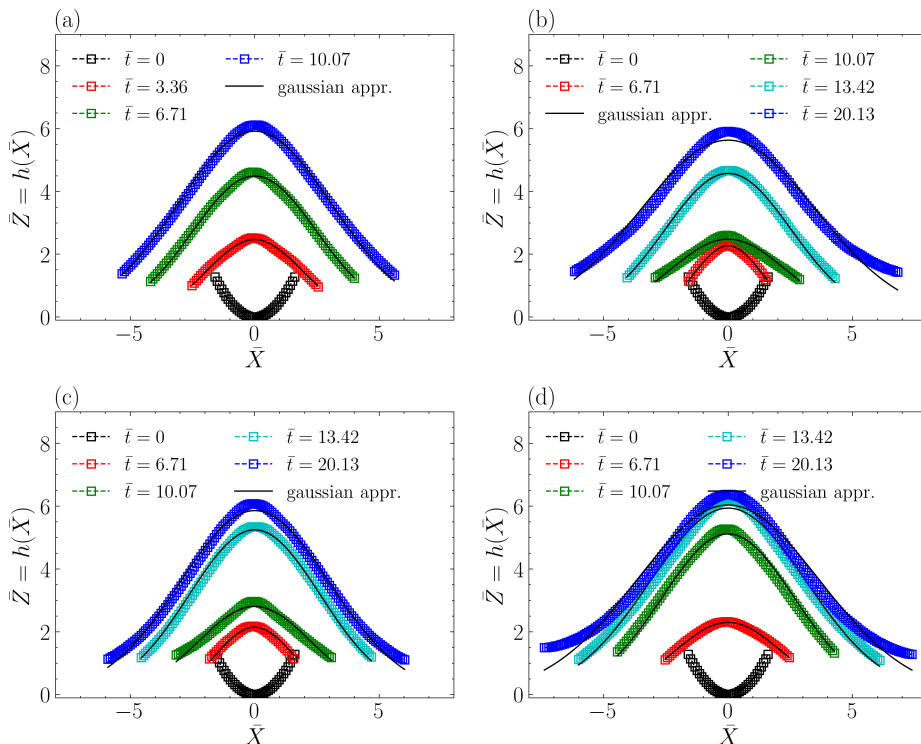


FIGURE 4. The evolution and the formation of the central dimple depicted by the variation of the 1D height profile as a function of time for various surface temperatures (a) $T_s = 300^\circ K$, (b) $T_s = 353^\circ K$, (c) $T_s = 423^\circ K$, (d) $T_s = 473^\circ K$. The horizontal and vertical axis \bar{X} , \bar{Z} represents the non-dimensional cartesian coordinates.

the \bar{X} - \bar{Z} plane using equation (3.27) and the linear approximation of the z-component of the velocity field \bar{u}_z satisfying the boundary condition given by equation (3.15), (3.16) owing to the very small value of ϵ prior to dimple formation. The black dotted line represents the $\bar{Z} = 0.5$ horizontal plane parallel to $\bar{X} - \bar{Y}$ plane. Fig. 3(c) represents the axisymmetric pressure field in the $\bar{X} - \bar{Y}$ plane for $0 < \bar{Z} < 1$. Fig. 3(d) represents the axisymmetric velocity field in a plane given by $\bar{Z} = 0.5$ parallel to the $\bar{X} - \bar{Y}$ plane according to equation (3.27). The velocity field denotes radially outward air flow from the center representing the air draining out due to the impacting drop. The dimple starts to form when the air pressure at the center of the dimple becomes greater than the capillary pressure.

$$p|_{\bar{r}=0} > p_{cap} \quad (3.28)$$

The non dimensional pressure at the dimple centre is $\bar{p}(\bar{r} = 0) = 3$ from equation (3.26). Using the scale transformation between p and \bar{p} i.e., $p = \bar{p}\mu_a V_0 / (R_0 \epsilon^2)$ we have

$$\frac{3\mu_a V_0}{R_0 \epsilon^2} > \frac{2\sigma}{R_0} \quad (3.29)$$

On simplifying further and solving the inequality for ϵ we have

$$\epsilon < \sqrt{\frac{3\mu_a V_0}{2\sigma_{aw}}} \quad (3.30)$$

Therefore the critical value of ϵ before central dimple formation begins is

$$\epsilon_{crit} = \sqrt{\frac{3}{2}}Ca^{1/2} \quad (3.31)$$

where $Ca = \mu_a V_0 / \sigma_{aw}$ is the capillary number. The actual central dimple thickness profile evolution was measured from high speed interferometric imaging as shown in Fig.4. Fig. 4(a), 4(b), 4(c) and 4(d) represents the central dimple evolution with time for substrate temperature $300^\circ K$, $353^\circ K$, $423^\circ K$ and $473^\circ K$ respectively. The time coordinate has been renormalized appropriately for non-dimensional purposes as $\bar{t} = tV_0/(R_0\epsilon)$. The $\bar{t} = 0$ is referenced with respect to the closest approach of the droplet to the substrate prior to dimple formation, i.e. the time instant when $\epsilon = 1.146 \times 10^{-3}$. The shape of the droplet close to the origin of coordinates is concave up shape represented by equation (3.4) locally (quadratic profile). Since at $\bar{t} = 0$ $\epsilon < \epsilon_{crit}$, the pressure below the droplet is greater than the capillary pressure (refer to equation 3.28-3.31). The excess pressure causes radial air flow outwards as depicted in Fig. 3(b) and 3(d). In addition to the flow as a response to the increase in air pressure, the air-water interface deforms and its curvature changes as depicted in Fig. 4 at different time instants labelled by \bar{t} . We discover that the central air dimple evolution profiles can be approximated by a gaussian curve (refer to black curves in Fig.4) of the form

$$h(\bar{r}) = ae^{-\bar{r}^2/2\sigma^2} \quad (3.32)$$

where a characterizes the dimple thickness at the origin and σ characterizes the spread of the profile (the standard deviation in terms of gaussian), \bar{r} is the radial coordinate. The black curves in Fig.4 depicts the gaussian approximation to the central dimple profile evolution at different time instants. Substituting equation (3.32) in equation (3.24) we have

$$\frac{\partial \bar{p}}{\partial \bar{r}} = -\frac{6}{a^3} \bar{r} e^{3\bar{r}^2/2\sigma^2} \quad (3.33)$$

Integrating with respect to \bar{r} we have

$$\bar{p}(\bar{r}) = \bar{p}(0) - \int_0^{\bar{r}} \frac{6}{a^3} \bar{r} e^{3\bar{r}^2/2\sigma^2} d\bar{r} \quad (3.34)$$

$$\bar{p}(\bar{r}) = \bar{p}(0) - \frac{2\sigma^2}{a^3} e^{3\bar{r}^2/2\sigma^2} \quad (3.35)$$

Further on substituting equation (3.32) and (3.33) in equation (3.17) the radial velocity field becomes

$$\bar{u}_r = -\frac{6}{a^3} \bar{r} e^{3\bar{r}^2/2\sigma^2} \left(\frac{\bar{z}^2}{2} - \frac{\bar{z}}{2} a e^{-\bar{r}^2/2\sigma^2} \right) \quad (3.36)$$

The radial velocity field variation with time is plotted as a contour field in Fig. 5, Fig. 6, Fig. 7 and Fig. 8 for substrate temperature $300^\circ K$, $353^\circ K$, $423^\circ K$ and $473^\circ K$ respectively. Fig. 5 depicts the central dimple evolution and the radial velocity field contours and vectors in the \bar{Z} - \bar{X} plane. Fig. 5(a), 5(b) and 5(c) represents the dimple evolution at three different time instants $\bar{t} = 3.36$, $\bar{t} = 6.71$ and $\bar{t} = 10.07$. The red solid curve depicts the air-dimple interface evolution as a function of time according to equation (3.32) where a and σ are function of time. The time $\bar{t} = 10.07$ corresponds to the instant where the dimple is at its maximum height and has attained a steady profile. It is interesting to note that the maximum radial velocity scale is decreasing as time progresses from a value of 0.324 at $\bar{t} = 3.36$ to approximately 0.1215 at $\bar{t} = 10.07$.

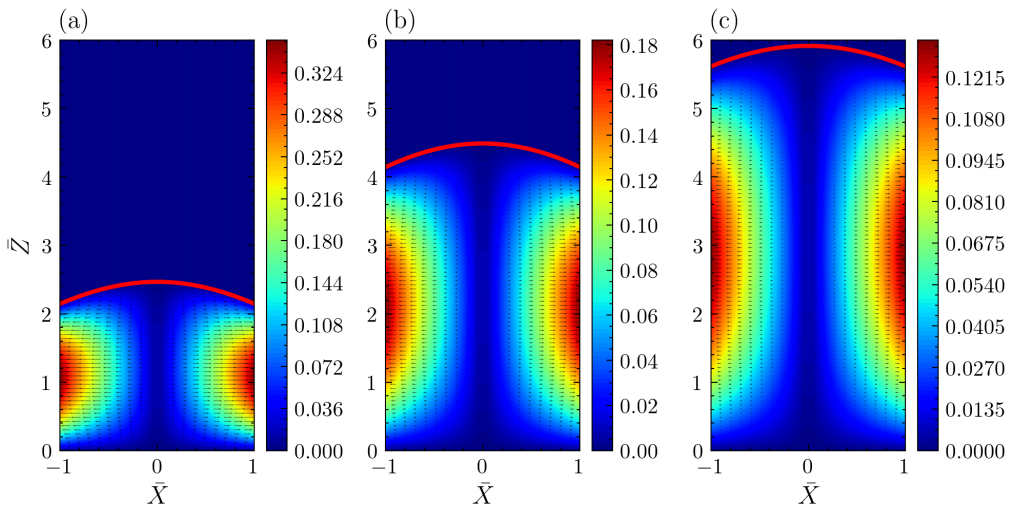


FIGURE 5. The asymptotic radial velocity field evolution as a function of time in the central air dimple region depicted as a contour map for substrate temperature $T_s = 300^\circ K$ at (a) $\bar{t} = 3.36$, (b) $\bar{t} = 6.71$, and (c) $\bar{t} = 10.07$.

This is in accordance with the continuity equation that as time progresses the velocity profiles becomes elongated and narrower (refer to the arrows marked in Fig. 5 that shows the velocity profile evolution). Fig. 6 depicts the dynamic dimple evolution through time varying vector fields and the contour maps for impact on substrate at temperature $T_s = 353^\circ K$. Fig. 6(a), 6(b), 6(c) and 6(d) represents the various non-dimensional time instants represented by $\bar{t} = 6.71$, $\bar{t} = 10.07$, $\bar{t} = 13.42$ and $\bar{t} = 20.13$ respectively. Similar vector fields and contours are plotted for other substrate temperatures in Fig. 7 ($423^\circ K$) and Fig. 8 ($473^\circ K$) respectively. Notice that in all substrate temperature the non-dimensional radial velocity scales are of similar order of magnitude indicating the dynamics in the central dimple region is inherently independent of substrate temperature in the range considered in this work. The maximum central dimple thickness however is weakly dependent on the substrate temperature. The region around the central dimple consists of the peripheral air disc where the air thickness is of the order of $100nm$. Small perturbations at the air-water interface develops in the peripheral air disc (discussed in detail in a later section) that results in asymmetric air layer dewetting/rupture (or it could be called wetting of the droplet with the substrate).

As the air between the drop and the substrate drains and thins out, structures appear in the peripheral air disc. The air thickness in the disc region reaches close to mean free path before first point of contact between the drop and the substrate. The first point of contact is designated as the air layer rupture point. The time it takes to form the rupture point is known as the rupture time scale and the radial distance between the rupture location and the origin of coordinates is known as the rupture radius. The rupture time scale increases with increases in substrate temperature as can be observed in the box-plot depicted in Fig. 9(a). We also observe correspondingly in Fig. 9(b) that the rupture radius increases with the substrate temperature T_s . The green horizontal line in the box plot denotes the median value of the rupture time and rupture radius. The rupture time and rupture radius are measured in μs and μm respectively. Corresponding to ϵ_{crit} from

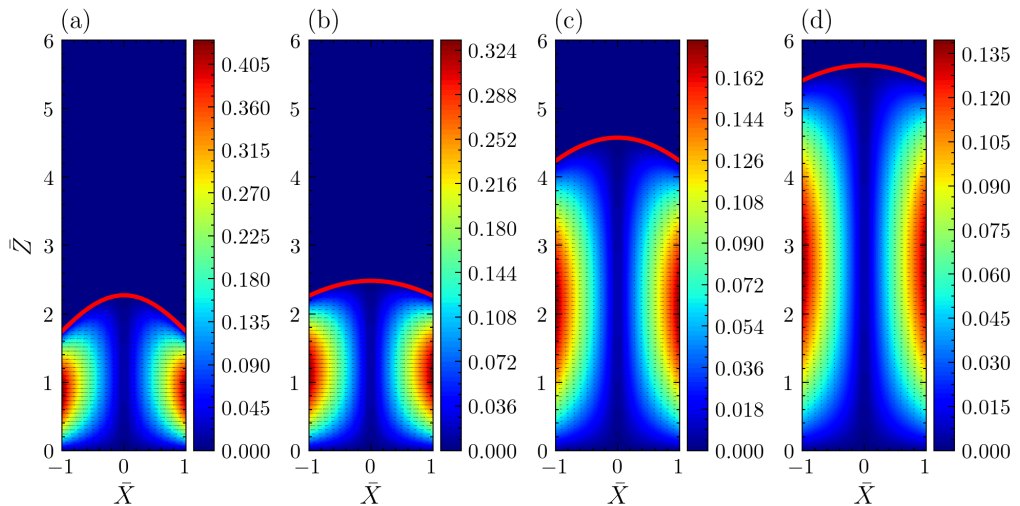


FIGURE 6. The asymptotic radial velocity field evolution as a function of time in the central air dimple region depicted as a contour map for substrate temperature $T_s = 353^\circ K$ at (a) $\bar{t} = 6.71$, (b) $\bar{t} = 10.07$, (c) $\bar{t} = 13.42$, and (d) $\bar{t} = 20.13$.

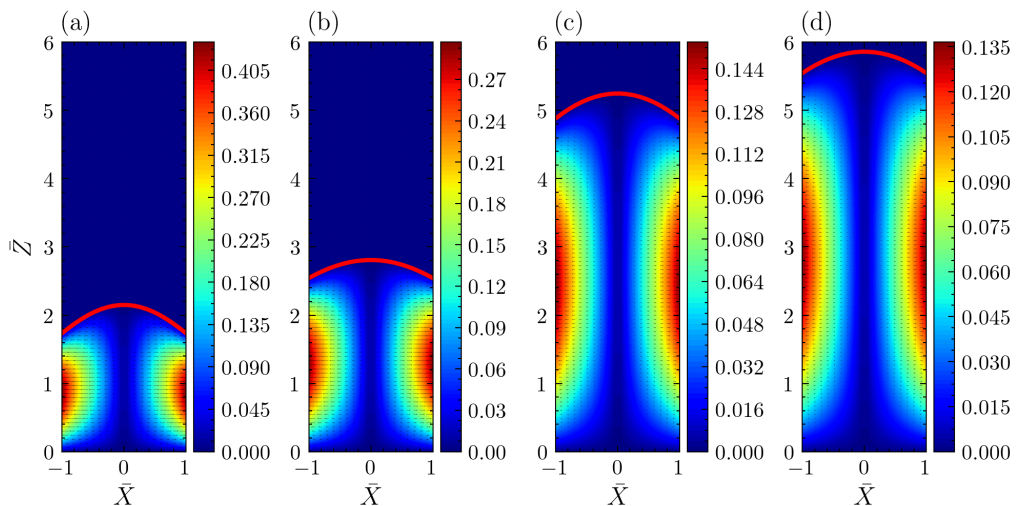


FIGURE 7. The asymptotic radial velocity field evolution as a function of time in the central air dimple region depicted as a contour map for substrate temperature $T_s = 423^\circ K$ at (a) $\bar{t} = 6.71$, (b) $\bar{t} = 10.07$, (c) $\bar{t} = 13.42$, and (d) $\bar{t} = 20.13$.

equation (3.31) the critical air layer thickness prior to dimple formation is given as

$$h_{crit} = \sqrt{\frac{3}{2}} Ca^{1/2} R_0 \quad (3.37)$$

where $Ca = \mu_a V_0 / \sigma_{aw}$ is the capillary number and R_0 is the impacting droplet radius. The capillary number depends on the temperature and varies with temperature due to surface tension dependence on temperature as $\sigma_{aw} = a - bT_s$. Incorporating the linear surface tension dependence on temperature, the critical thickness from equation (3.37)

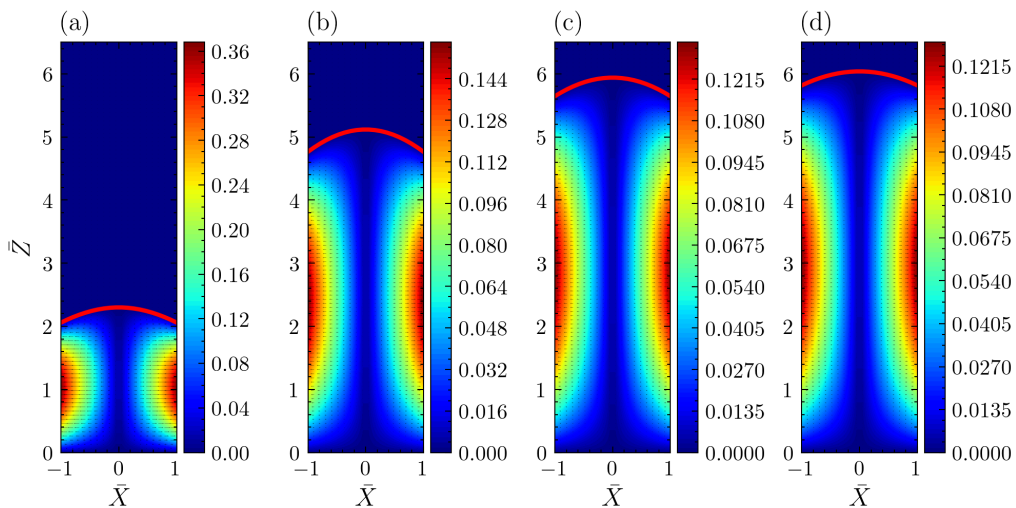


FIGURE 8. The asymptotic radial velocity field evolution as a function of time in the central air dimple region depicted as a contour map for substrate temperature $T_s = 473^\circ K$ at (a) $\bar{t} = 6.71$, (b) $\bar{t} = 10.07$, (c) $\bar{t} = 13.42$, and (d) $\bar{t} = 20.13$.

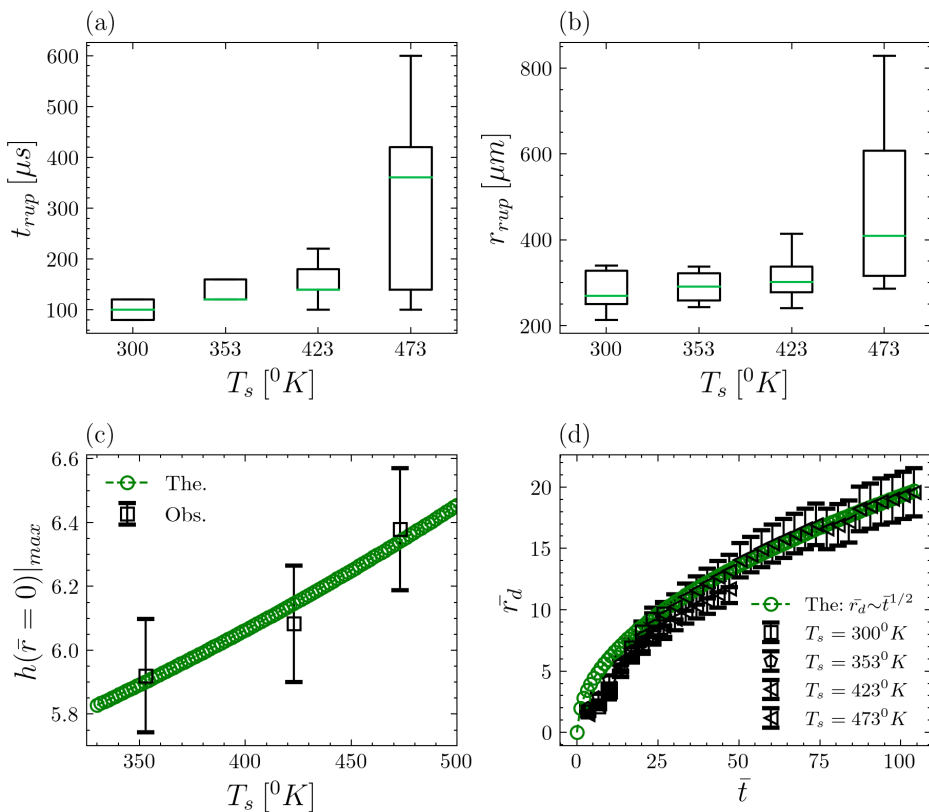


FIGURE 9. (a) The air layer rupture time as a function of substrate temperature. (b) The air layer rupture radius as a function of substrate temperature. (c) The central dimple maximum thickness as a function of substrate temperature. (d) The radial air disc expansion as a function of time.

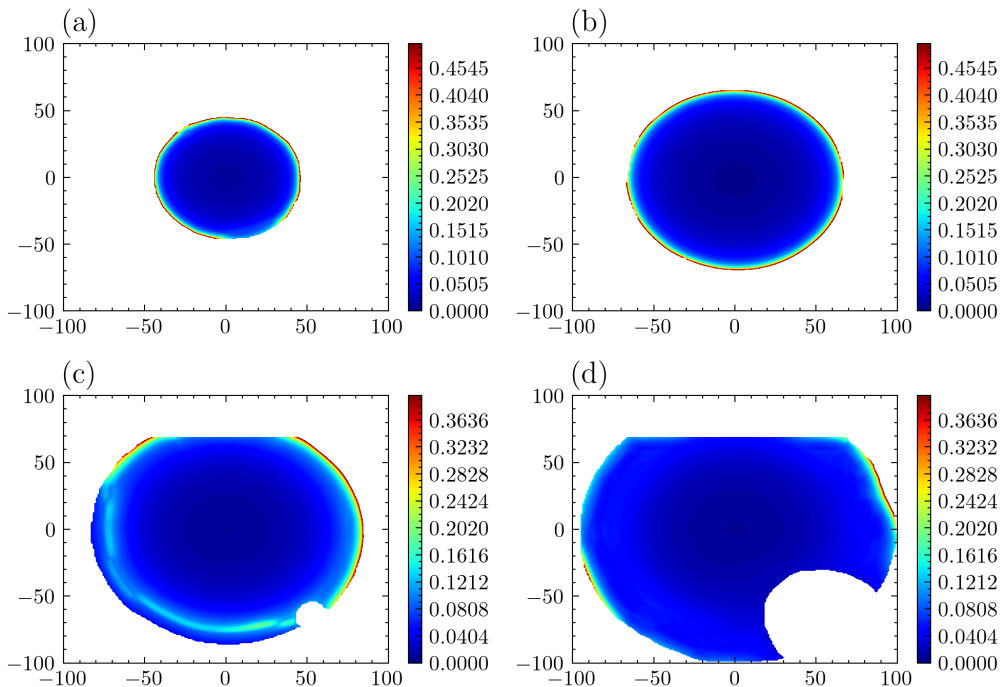


FIGURE 10. The 2d knudsen field evolution as a function of time for substrate temperature $T_s = 300^\circ K$ at (a) $\bar{t} = 6.71$, (b) $\bar{t} = 10.07$, (c) $\bar{t} = 13.42$, and (d) $\bar{t} = 16.78$.

becomes

$$h_{crit} = \sqrt{\frac{3\mu V_0}{2(a - bT_s)}} R_0 \quad (3.38)$$

In general the maximum central dimple thickness is proportional to the critical thickness given by equation (3.38) as the pressure at the center of the dimple that causes the deformation of the droplet interface is correlated to ϵ_{crit} and hence to h_{crit} . Therefore, the maximum dimple thickness at $\bar{r} = 0$ has a temperature dependence similar to equation (3.38) i.e. $h(\bar{r} = 0)|_{max} \sim 1/\sqrt{a - bT_s}$. Fig. 9(c) compares the experimental central dimple maximum thickness with the theoretical scaling of $h(\bar{r} = 0)|_{max}$. The experimental values agrees with the theoretical scale within the experimental uncertainty. The lubrication pressure prior to dimple formation is given by

$$F_{lub} = \frac{2\pi\mu V_0 R_0}{\epsilon} \int_0^{\bar{r}} \bar{p}(\bar{r}) \bar{r} d\bar{r} \quad (3.39)$$

Using the value of non-dimensional pressure from equation (3.26) in equation (3.39) we have

$$F_{lub} = \frac{6\pi\mu V_0 R_0}{\epsilon} \int_0^{\bar{r}} \frac{\bar{r} d\bar{r}}{1 + \bar{r}^2/2} = \frac{6\pi\mu V_0 R_0}{\epsilon} \int_0^\infty \frac{\bar{r} d\bar{r}}{1 + \bar{r}^2/2} = \frac{6\pi\mu V_0 R_0}{\epsilon} \quad (3.40)$$

The lubrication force varies inversely as ϵ and hence blows up in the limit $\epsilon \rightarrow 0$. Physically for impact of solid objects the singularity is real and the singularity cutoff occurs through non-continuum mechanics. For the present case of impact of liquid droplets the singularity at the center of coordinates is avoided due to the deforming nature of the air water interface. i.e., for drop impacts on solids or liquids the singularity is never reached at the

center of coordinates due to dimple formation mechanisms discussed above. For impact of drops on solids and liquids at moderate to low impact energies the system approaches the mathematical singularity in the peripheral air disc region. However, physically the singularity is never reached and is cut off by non-continuum 3d structures that occurs due to balance of capillary and van der Waals interaction. Using $\epsilon = h_0/R_0$ in (3.40) the lubrication pressure prior to dimple formation becomes

$$F_{lub} = \frac{6\pi\mu V_0 R_0^2}{h_0} \quad (3.41)$$

Applying Newtons second law provides us the dynamical equation of motion for the impacting droplet

$$F_{mg} - F_{lub} - F_v = m \frac{dV_{cm}}{dt} \quad (3.42)$$

At the time just before droplet starts to decelerate (i.e., dV_{cm}/dt changes sign), we have $dV_{cm}/dt = 0$. Therefore equation (3.42) becomes

$$\frac{4}{3}\pi\rho_w R_0^3 g - \frac{6\pi\mu V_0 R_0^2}{h_0} - 6\pi\mu R_0 V_0 = 0 \quad (3.43)$$

On simplifying and solving for h_0 we have

$$h_0 = \frac{9\mu_a V_0 R_0^2}{2R_0^3 g (\rho_w - \rho_a) - 9\mu_a V_0 R_0} \quad (3.44)$$

Writing equation (3.44) in a non-dimensional manner we have

$$\epsilon = \frac{h_0}{R_0} = \frac{9Ca}{2Bo - 9Ca} \quad (3.45)$$

where $Ca = \mu_a V_0 / \sigma_{aw}$, and $Bo = (\rho_w - \rho_a) R_0^2 g / \sigma_{aw}$ is the Bond number based on the droplet radius. The theoretical value of ϵ calculated using equation (3.45) is 1.25×10^{-3} agrees with the experimental value of 1.15×10^{-3} within the experimental uncertainty.

3.4. Estimating a scale for the dimple radius during dimple formation process

The bottom surface of the droplet and hence the air layer profile prior to dimple formation is given by (refer to equation (3.1))

$$h(r) = h_0 + R_0 \left(1 - \sqrt{1 - \left(\frac{r}{R_0} \right)^2} \right) \quad (3.46)$$

The condition for the air profile height becoming equal to h_{crit} at any particular radial coordinate r_{dimp} is given by

$$h_0 + R_0 \left(1 - \sqrt{1 - \left(\frac{r_{dimp}}{R_0} \right)^2} \right) = h_{crit} \quad (3.47)$$

The following inequalities are being satisfied in general impact scenarios. The condition for dimple to form in terms of air layer thickness is given by

$$h_0 < h_{crit} \quad (3.48)$$

Condition given by equation (3.48) holds due to the following inequality that states, in a general impact scenario where the droplet kinematic time scale of the interface is smaller

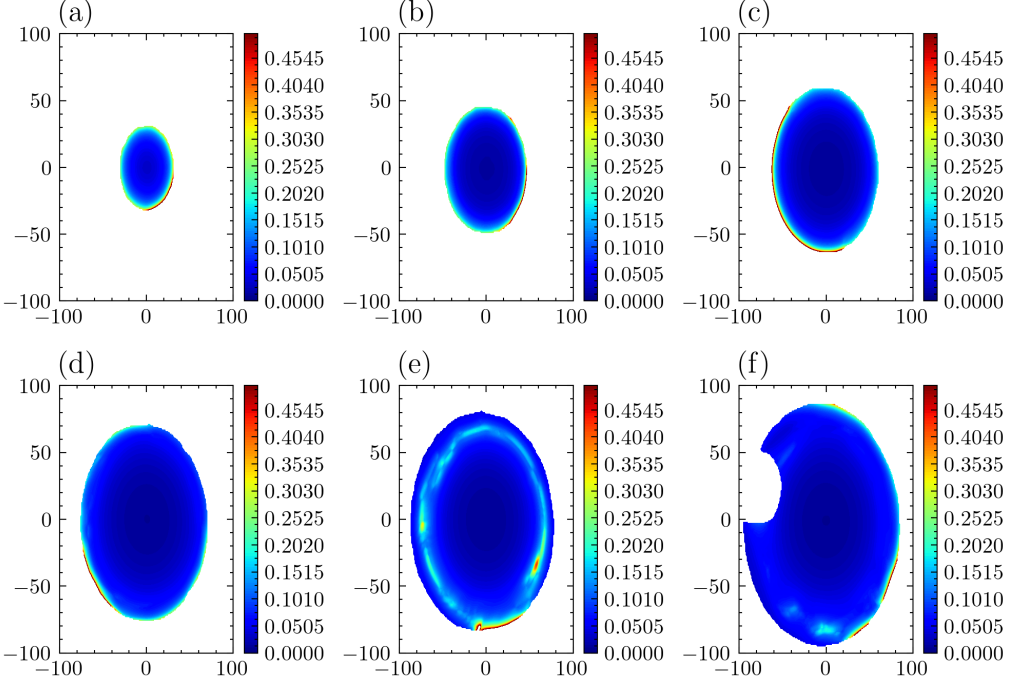


FIGURE 11. The 2d knudsen field evolution as a function of time for substrate temperature $T_s = 353^\circ K$ at (a) $\bar{t} = 6.71$, (b) $\bar{t} = 10.07$, (c) $\bar{t} = 13.42$, (d) $\bar{t} = 16.78$, (e) $\bar{t} = 20.13$, and (f) $\bar{t} = 23.49$.

than the capillary deformation time scale for the dimple formation, i.e.

$$\frac{h_{crit}}{V_0} < \sqrt{\frac{\rho R^3}{\sigma_{aw}}} \quad (3.49)$$

Rearranging equation (3.47) we have

$$1 - \sqrt{1 - \left(\frac{r_{dimp}}{R_0}\right)^2} = \frac{h_{crit} - h_0}{R_0} \quad (3.50)$$

Simplifying equation (3.50) we have

$$\sqrt{1 - \left(\frac{r_{dimp}}{R_0}\right)^2} = 1 - \left(\frac{h_{crit} - h_0}{R_0}\right) \quad (3.51)$$

The dimple radius therefore becomes

$$\frac{r_{dimp}}{R_0} = \sqrt{f(2-f)} \quad (3.52)$$

where

$$f = \frac{h_{crit} - h_0}{R_0} = \epsilon_{crit} - \epsilon \quad (3.53)$$

Note equation (3.52) predicts the approximate radius of the dimple during its formation stage. Therefore equation (3.52) should provide a dimple scale that should be greater than the radial length scale $R_0\epsilon^{1/2}$ and smaller than the maximum dimple radius, i.e.

$$R_0\epsilon^{1/2} < r_{dimp} < r_{dimp}|_{max} \quad (3.54)$$

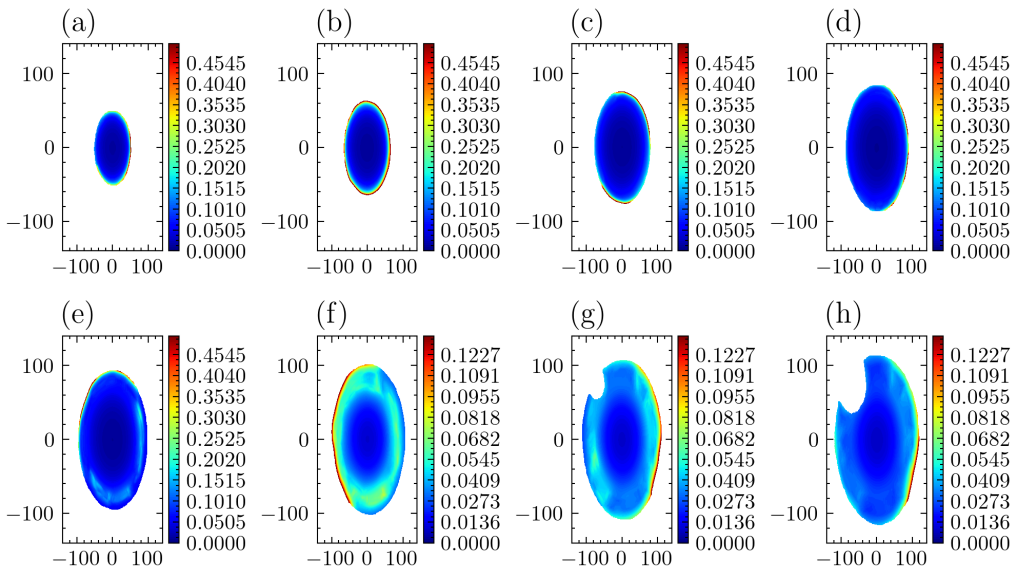


FIGURE 12. The 2d knudsen field evolution as a function of time for substrate temperature $T_s = 423^\circ K$ at (a) $\bar{t} = 10.07$, (b) $\bar{t} = 13.42$, (c) $\bar{t} = 16.78$, (d) $\bar{t} = 20.13$, (e) $\bar{t} = 23.49$, (f) $\bar{t} = 26.85$, (g) $\bar{t} = 30.20$, and (h) $\bar{t} = 33.56$.

Using the droplet radius R_0 and the value of ϵ and ϵ_{crit} from equation (3.45) and (3.27) respectively, the inequality provided in (3.54) is satisfied (the numerical translation of inequality (3.54) is $46\mu m < 141.77\mu m < 508.78\mu m$).

3.5. The expansion of the peripheral air disc

Based on the stokes approximation in the air layer region, the radial pressure gradient balances the viscous stresses and hence the radial momentum equation becomes

$$\frac{\partial p}{\partial r} = \mu_a \frac{\partial^2 u_r}{\partial z^2} \quad (3.55)$$

The pressure in the air layer is a superposition of various effects, however the capillary is the dominant scale once the dimple has formed. Therefore using the scales ($r \sim r_d$, $z \sim h_0$, $p \sim 2\sigma_{aw}/R_0$, $u_r \sim \langle V \rangle$ where $\langle V \rangle = dr_d/dt$ is the average expansion velocity of the air disc) in equation (3.54)

$$\frac{1}{r_d} \frac{2\sigma_{aw}}{R_0} \sim \mu_a \frac{\langle V \rangle}{h_0^2} = \frac{\mu_a}{h_0^2} \frac{dr_d}{dt} \quad (3.56)$$

$$r_d \frac{dr_d}{dt} \sim \frac{2\sigma_{aw}}{R_0} \frac{h_0^2}{\mu_a} \quad (3.57)$$

Integrating with respect to t we have

$$\int r_d dr_d \sim \int \frac{2\sigma_{aw}}{R_0} \frac{h_0^2}{\mu_a} dt \quad (3.58)$$

The radial disc expansion as a function of time becomes

$$r_d \sim 2\sqrt{\frac{\sigma_{aw} h_0^2}{R_0 \mu_a}} t^{1/2} \quad (3.59)$$

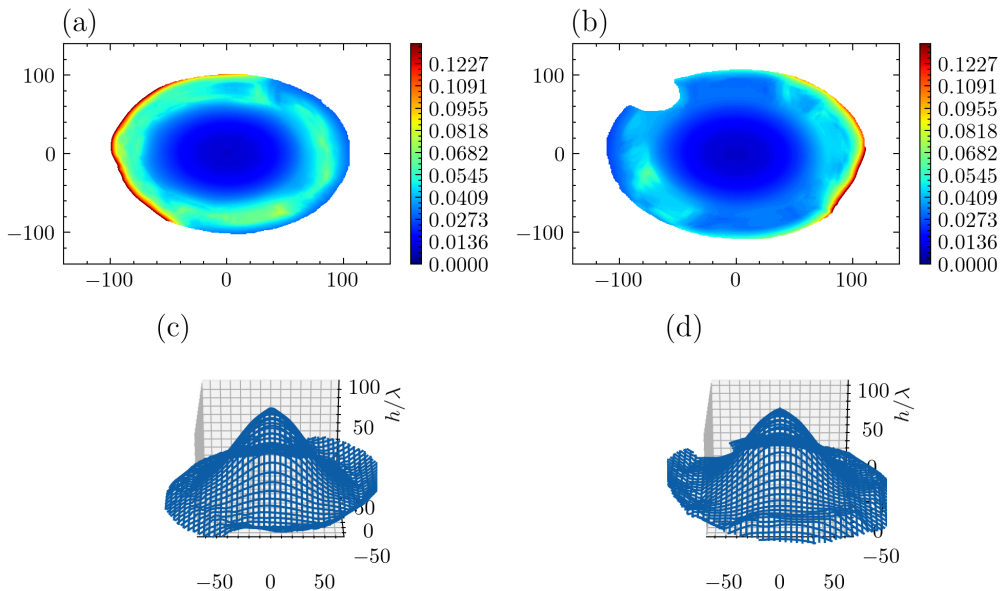


FIGURE 13. The 2d knudsen field evolution as a function of time for substrate temperature $T_s = 423^\circ K$ at (a) $\bar{t} = 26.85$, (b) $\bar{t} = 30.20$, (c) $\bar{t} = 26.85$, and (d) $\bar{t} = 30.20$.

Fig. 9(d) depicts the air disc expansion both theoretically and experimentally. The experimental and theoretical scales agrees within the experimental uncertainties. Notice that from equation (3.59) we have $r_d \sim t^{1/2}$ (Fig. 9(d)).

3.6. Spatial length scales in the peripheral air disc

The central air dimple is surrounded by a thin region that we refer to as the peripheral air disc. The peripheral air disc thickness is one order smaller than the central dimple thickness and the air layer thickness approaches the mean free path of air. The mean free path (λ_0) of the air molecules is given by

$$\lambda_0 = \frac{\mu_a}{p} \sqrt{\frac{\pi R_s T}{2}} \quad (3.60)$$

where μ_a is the air viscosity, and p , T , R_s denotes air pressure, temperature and specific gas constant respectively. At standard room temperature of $300^\circ K$ and pressure of $10^5 Pa$ the mean free path is approximately $67nm$. The ratio of the mean free path of the air to the local air layer thickness profile represents a 2D Knudsen field that we use to characterize the air layer beneath the impacting droplet. The Knudsen field is defined as

$$Kn = \frac{\lambda_0}{h} \quad (3.61)$$

where h represents the two dimensional air layer thickness profile. Note that the reciprocal of the Knudsen field represents a non-dimensional height profile measure. Fig. 10, 11, 12, 14 depicts the Knudsen field plotted for substrate temperature $300^\circ K$, $353^\circ K$, $423^\circ K$, $473^\circ K$ respectively. Comparing the Knudsen field, we can observe that the structures in the peripheral disc regions are distinct. A unique circular pattern is observed for all the temperature cases in the peripheral disc region where $Kn \sim \mathcal{O}(10^{-1})$ (refer to Fig. 10(c), 11(e), 12(f), 13(a), 14(e)). Subjected to very high values of Knudsen number in the peripheral air disc region the dynamics is governed by an interaction of continuum

and non-continuum effects. The flow field in the peripheral disc region lies in the slip flow and transition flow region in contrast to the central air dimple which lies entirely in the continuum regime. As the air beneath the impacting droplet drains out in the radial direction, the air-water interface at the bottom of the droplet is subjected to capillary waves. Capillary waves can form at the droplet interface if the capillary wavelength given by λ_c is smaller than equal to the droplet length scale R_0 , i.e.,

$$\lambda_c = \frac{\sigma_{aw}}{\rho_l V^2} \leq R_0 \quad (3.62)$$

where ρ_l is the density of the liquid, σ_{aw} is the air-water surface tension, and V_0 is the impact velocity. For the impact condition in this work the equality is satisfied and hence the interface is subjected to capillary perturbations. From Fig. 10-14 we observe that the Knudsen number before the first point of contact in certain locations of the peripheral air disc is one order larger than the mean free path ($Kn \sim 0.1$). Owing to a very small gap between the substrate and the droplet the pressure in the gap region is subjected to disjoining pressure that originates due to molecular interactions between surfaces. Derjaguin (Derjaguin & Churaev 1978) showed that the pressure field in such small gaps becomes anisotropic in comparison to the large scale isotropic pressure. The balance between disjoining and capillary pressure establishes the existence of new length scales for short time scales. The molecular (disjoining pressure term) and capillary interaction balance becomes (Roy *et al.* 2022)

$$\frac{A}{h_{pd}^3} \sim \frac{\sigma_{aw}}{R_0} \quad (3.63)$$

where A is the Hamaker's constant ($A \sim \mathcal{O}(4.76 \times 10^{-20} J)$), h_{pd} is the thickness in the peripheral air disc region. Solving for h_{pd} from equation (3.63) becomes

$$h_{pd} \sim \left(\frac{AR_0}{\sigma_{aw}} \right)^{1/3} \quad (3.64)$$

The wavelength corresponding to thin film instability is given by (Vrij 1966; Roy *et al.* 2022)

$$\lambda_{TF} \sim h^2 \left(\frac{\sigma_{aw}}{A} \right)^{1/2} \quad (3.65)$$

where h represents the air layer thickness in the peripheral air disc region. Substituting h_{pd} from equation (3.64) in equation (3.65) we have

$$\lambda_{TF} \sim \left(\frac{AR_0^4}{\sigma_{aw}} \right)^{2/3} \left(\frac{\sigma_{aw}}{A} \right)^{1/2} \quad (3.66)$$

Simplifying equation (3.66) we get

$$\lambda_{TF} \sim \left(\frac{AR_0^4}{\sigma_{aw}} \right)^{1/6} \quad (3.67)$$

The theoretical thin film instability length scale predicted from equation (3.67) corroborates with the experimental measured scales in the peripheral disc region. The theoretical scale comes out to be of the order of $\lambda_{TF}^{th} \sim 10 \mu m$ while the mean of the experimental measured length scale is $11.89 \mu m$ with a standard deviation of $1.79 \mu m$. The structures we discover in the peripheral air disc region are the experimental realizations of the kink mode of contact discussed numerically in some recent articles (de Ruiter *et al.* 2015b; Chubynsky *et al.* 2020).

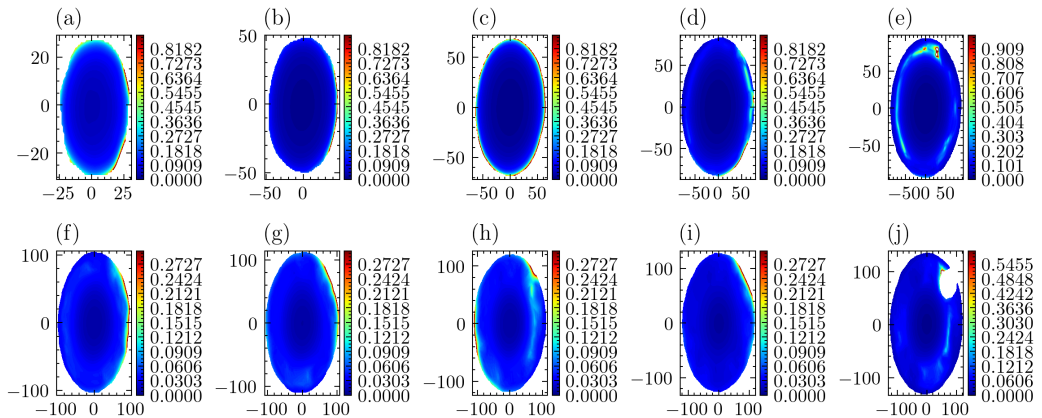


FIGURE 14. The 2d knudsen field evolution as a function of time for substrate temperature $T_s = 473^\circ K$ at (a) $\bar{t} = 3.36$, (b) $\bar{t} = 6.71$, (c) $\bar{t} = 10.07$, (d) $\bar{t} = 13.42$, (e) $\bar{t} = 16.78$, (f) $\bar{t} = 20.13$, (g) $\bar{t} = 23.49$, (h) $\bar{t} = 26.85$, (i) $\bar{t} = 30.20$, and (j) $\bar{t} = 33.56$.

4. Conclusion

In conclusion, we study the air layer dynamics beneath an impacting droplet on a heated substrate. We show that a gaussian profile could represent the evolving central air dimple profile. The geometry of the dimple depends on the substrate temperature very weakly and is a function of the impact Weber number majorly. Further, we observe that the air layer rupture time scale and rupture radius increase with an increase in substrate temperature slowly. We characterize the entire air layer profile beneath the droplet by a time-varying Knudsen field. We show that a unified treatment of continuum and non-continuum mechanics is required to comprehend the flow field and the local anisotropic 3d structures observed in the peripheral air disc. The airflow dynamics in the central dimple region lies within the continuum stokes regime, whereas the peripheral air disc falls within the non-continuum slip flow and transition regime owing to the large Knudsen number. However, the average air disc expansion length scale on an average could be explained based on the continuum stokes approximation. We show that the structures observed in the peripheral air disc provide the mechanism for the film and kink contact modes between the droplet and the substrate. The structures in the peripheral disc region initiate asymmetric contact between the droplet and the substrate. The structures in the peripheral air disc occur due to the asymptotic effects of Van der Waals and capillary interactions. Future investigations at the intersection of classical continuum mechanics and statistical mechanics are required to probe the mechanisms and the associated spatiotemporal length scales in the peripheral air disc in sufficient detail.

Declaration of Interests

The authors declare no conflict of interest.

REFERENCES

- ANDRADE, R, SKURTYS, O & OSORIO, F 2013 Drop impact behavior on food using spray coating: Fundamentals and applications. *Food research international* **54** (1), 397–405.
- BREITENBACH, JAN, ROISMAN, ILIA V & TROPEA, CAMERON 2017 Heat transfer in the film boiling regime: Single drop impact and spray cooling. *International Journal of Heat and Mass Transfer* **110**, 34–42.
- BREITENBACH, JAN, ROISMAN, ILIA V & TROPEA, CAMERON 2018 From drop impact physics to spray cooling models: a critical review. *Experiments in Fluids* **59**, 1–21.
- CHUBYSKY, MYKYTA V, BELOUSOV, KIRILL I, LOCKERBY, DUNCAN A & SPRITTLES, JAMES E 2020 Bouncing off the walls: the influence of gas-kinetic and van der waals effects in drop impact. *Physical Review Letters* **124** (8), 084501.
- DANIEL, DAN, TIMONEN, JAAKKO VI, LI, RUOPING, VELLING, SENECA J & AIZENBERG, JOANNA 2017 Oleoplaning droplets on lubricated surfaces. *Nature Physics* **13** (10), 1020–1025.
- DE RUITER, JOLET, LAGRAAUW, RUDY, VAN DEN ENDE, DIRK & MUGELE, FRIEDER 2015 Wettability-independent bouncing on flat surfaces mediated by thin air films. *Nature physics* **11** (1), 48–53.
- DERJAGUIN, BV & CHURAEV, NV 1978 On the question of determining the concept of disjoining pressure and its role in the equilibrium and flow of thin films. *Journal of Colloid and Interface Science* **66** (3), 389–398.
- DRISCOLL, MICHELLE M & NAGEL, SIDNEY R 2011 Ultrafast interference imaging of air in splashing dynamics. *Physical review letters* **107** (15), 154502.
- DE GOEDE, THIJS C, DE BRUIN, KARLA G, SHAHIDZADEH, NOUSHINE & BONN, DANIEL 2019 Predicting the maximum spreading of a liquid drop impacting on a solid surface: Effect of surface tension and entrapped air layer. *Physical review fluids* **4** (5), 053602.
- HICKS, PETER D & PURVIS, RICHARD 2010 Air cushioning and bubble entrapment in three-dimensional droplet impacts. *Journal of Fluid Mechanics* **649**, 135–163.
- HICKS, PETER D & PURVIS, RICHARD 2011 Air cushioning in droplet impacts with liquid layers and other droplets. *Physics of fluids* **23** (6), 062104.
- KAI, LI & KEMAO, QIAN 2010 Fast frequency-guided sequential demodulation of a single fringe pattern. *Optics letters* **35** (22), 3718–3720.
- KITAGAWA, KATSUICHI 2013 Thin-film thickness profile measurement by three-wavelength interference color analysis. *Applied optics* **52** (10), 1998–2007.
- KOLINSKI, JOHN M, RUBINSTEIN, SHMUEL M, MANDRE, SHREYAS, BRENNER, MICHAEL P, WEITZ, DAVID A & MAHADEVAN, L 2012 Skating on a film of air: drops impacting on a surface. *Physical review letters* **108** (7), 074503.
- LANGLEY, KENNETH, LI, ER QIANG & THORODDSEN, SIGURDUR T 2017 Impact of ultra-viscous drops: air-film gliding and extreme wetting. *Journal of Fluid Mechanics* **813**, 647–666.
- LANGLEY, KR & THORODDSEN, SIGURDUR T 2019 Gliding on a layer of air: impact of a large-viscosity drop on a liquid film. *Journal of Fluid Mechanics* **878**, R2.
- LI, EQ, VAKARELSKI, IVAN URIEV & THORODDSEN, SIGURDUR T 2015 Probing the nanoscale: the first contact of an impacting drop. *Journal of Fluid Mechanics* **785**, R2.
- LIMOZIN, LAURENT & SENGUPTA, KHEYA 2009 Quantitative reflection interference contrast microscopy (ricm) in soft matter and cell adhesion. *ChemPhysChem* **10** (16), 2752–2768.
- LOHSE, DETLEF 2022 Fundamental fluid dynamics challenges in inkjet printing. *Annual review of fluid mechanics* **54**, 349–382.
- ROY, DURBAR, PANDEY, KHUSHBOO, BANIK, MENEKA, MUKHERJEE, RABIBRATA & BASU, SAPTARSHI 2019 Dynamics of droplet impingement on bioinspired surface: insights into spreading, anomalous stickiness and break-up. *Proceedings of the Royal Society A* **475** (2229), 20190260.
- ROY, DURBAR, RAO, SRINIVAS S & BASU, SAPTARSHI 2022 Droplet impact on immiscible liquid pool: Multi-scale dynamics of entrapped air cushion at short timescales. *Physics of Fluids* **34** (5), 052004.
- ROY, DURBAR, SOPHIA, M & BASU, SAPTARSHI 2023 On the mechanics of droplet surface crater during impact on immiscible viscous liquid pool. *Journal of Fluid Mechanics* **955**, A27.
- DE RUITER, JOLET, VAN DEN ENDE, DIRK & MUGELE, FRIEDER 2015a Air cushioning in droplet

- impact. ii. experimental characterization of the air film evolution. *Physics of fluids* **27** (1), 012105.
- DE RUITER, JOLET, MUGELE, FRIEDER & VAN DEN ENDE, DIRK 2015*b* Air cushioning in droplet impact. i. dynamics of thin films studied by dual wavelength reflection interference microscopy. *Physics of fluids* **27** (1), 012104.
- DE RUITER, JOLET, OH, JUNG MIN, VAN DEN ENDE, DIRK & MUGELE, FRIEDER 2012 Dynamics of collapse of air films in drop impact. *Physical review letters* **108** (7), 074505.
- SCHNEIDER, CAROLINE A, RASBAND, WAYNE S & ELICEIRI, KEVIN W 2012 Nih image to imagej: 25 years of image analysis. *Nature methods* **9** (7), 671–675.
- SUGIYAMA, MASASHI, OGAWA, HIDEMITSU, KITAGAWA, KATSUICHI & SUZUKI, KAZUYOSHI 2006 Single-shot surface profiling by local model fitting. *Applied Optics* **45** (31), 7999–8005.
- THORODDSEN, SIGURDUR T, ETOH, TAKEHARU GOJI & TAKEHARA, KOHSEI 2008 High-speed imaging of drops and bubbles. *Annu. Rev. Fluid Mech.* **40**, 257–285.
- THORODDSEN, SIGURDUR T, TAKEHARA, KOHSEI & ETOH, TG 2012 Micro-splashing by drop impacts. *Journal of Fluid Mechanics* **706**, 560–570.
- VAN ROSSUM, GUIDO & DRAKE, FRED L. 2009 *Python 3 Reference Manual*. Scotts Valley, CA: CreateSpace.
- VRIJ, AGIENUS 1966 Possible mechanism for the spontaneous rupture of thin, free liquid films. *Discussions of the Faraday Society* **42**, 23–33.
- WANG, HAIXIA & KEMAO, QIAN 2009 Frequency guided methods for demodulation of a single fringe pattern. *Optics Express* **17** (17), 15118–15127.
- WIJSHOFF, HERMAN 2018 Drop dynamics in the inkjet printing process. *Current opinion in colloid & interface science* **36**, 20–27.
- WOOLF, DK, LEIFER, IS, NIGHTINGALE, PD, RHEE, TS, BOWYER, P, CAULLIEZ, GUILLEMETTE, DE LEEUW, G, LARSEN, SØREN EJLING, LIDICOAT, M, BAKER, J & OTHERS 2007 Modelling of bubble-mediated gas transfer: Fundamental principles and a laboratory test. *Journal of Marine Systems* **66** (1-4), 71–91.
- WORTHINGTON, ARTHUR MASON 1877 Xxviii. on the forms assumed by drops of liquids falling vertically on a horizontal plate. *Proceedings of the royal society of London* **25** (171-178), 261–272.
- WORTHINGTON, ARTHUR MASON 1883 On impact with a liquid surface. *Proceedings of the Royal Society of London* **34** (220-223), 217–230.
- WORTHINGTON, ARTHUR MASON & COLE, REGINALD SORRÈ 1897 V. impact with a liquid surface, studied by the aid of instantaneous photography. *Philosophical Transactions of the Royal Society of London. Series A, Containing Papers of a Mathematical or Physical Character* (189), 137–148.
- WORTHINGTON, ARTHUR MASON & COLE, REGINALD SORRÈ 1900 Iv. impact with a liquid surface studied by the aid of instantaneous photography. paper ii. *Philosophical Transactions of the Royal Society of London. Series A, Containing Papers of a Mathematical or Physical Character* **194** (252-261), 175–199.
- WORTHINGTON, ARTHUR M & OTHERS 1877 A second paper on the forms assumed by drops of liquids falling vertically on a horizontal plate. *Proc. R. Soc. London* **25**, 498–503.
- XU, LEI, ZHANG, WENDY W & NAGEL, SIDNEY R 2005 Drop splashing on a dry smooth surface. *Physical review letters* **94** (18), 184505.
- YARIN, ALEXANDER L 2006 Drop impact dynamics: splashing, spreading, receding, bouncing. . . . *Annu. Rev. Fluid Mech.* **38**, 159–192.
- YARIN, ALEXANDER L, ROISMAN, ILIA V & TROPEA, CAMERON 2017 *Collision phenomena in liquids and solids*. Cambridge University Press.